

GCM Simulations of the Three-Dimensional Propagation of Stationary Waves

SONG YANG*

Atmospheric and Environmental Research, Inc., Cambridge, Massachusetts

WILLIAM J. GUTOWSKI, JR.

Department of Geologic and Atmospheric Sciences, Iowa State University, Ames, Iowa

(Manuscript received 12 November 1992, in final form 11 August 1993)

ABSTRACT

Plumb's formulation of the stationary wave activity flux is used to determine how well versions of the GFDL and NCAR general circulation models simulate the sources, sinks, and horizontal propagation of atmospheric stationary waves, which play an important role in determining regional climate. The wave activity flux provides insight into the simulation of nondynamic as well as dynamic processes in these models. Model performances for current climate simulations are evaluated with respect to NMC analyses averaged over 1978–1990.

The models fare best when the stationary wave forcing is strongest, that is, in the wintertime Northern Hemisphere, where they reproduce the observed three-branch structure of upward wave activity flux. For the Northern Hemisphere summer and the Southern Hemisphere in both summer and winter, the models show less agreement with observations, although they do simulate the generally downward flux observed during Northern Hemisphere summer, which the analysis suggests is caused by convection. CO₂-doubling changes in the wave activity flux show little consistency between the two models. The analysis suggests that accurate modeling of stationary wave activity flux is strongly dependent on diabatic forcing, especially that occurring in storm tracks. Improving the simulation of stationary wave activity forcing requires a much better understanding of the physics governing storm tracks and latent heat release in the atmosphere, so that improvements in stationary wave simulation in these models will not occur by simply increasing model resolution.

1. Introduction

General circulation models (GCMs) are useful tools for studying potential climate change (Houghton et al. 1990) and for understanding mechanisms producing climate changes in past records (e.g., Kutzbach and Guetter 1986). Because GCMs simulate the three-dimensional climate, they can provide insight into regional climate change, a capability that is invaluable for evaluating the impact of climate change on human activities. However, a number of factors, such as limits to model resolution and inaccurate parameterization of subgrid-scale phenomena, restrict the accuracy of GCM simulations of regional climate change, as suggested by comparisons between GCMs in their simulations of soil moisture (Kellogg and Zhao 1988), temperature and precipitation (Grotch and MacCracken 1991), and surface energy balances (Gutowski et al.

1991). Improving regional climate simulation requires, in part, analyzing of the capability of models to simulate the myriad processes involved.

The atmosphere's circulation is an important contributor to regional climate through its horizontal transports of energy, moisture, and momentum. Atmospheric stationary waves can play a significant role in establishing regional circulation dynamics, and so their simulation by GCMs should be evaluated for fidelity to observed flow and consistency among models. Here we compare stationary wave dynamics in two GCMs and in observations using the stationary wave activity flux derived by Plumb (1985).

Plumb (1985) contends that the stationary wave activity flux is a more revealing and less misleading diagnostic compared to frequently applied energetic arguments for analyzing wave behavior in the atmosphere. The wave activity flux is intimately related to the underlying Hamiltonian structure of atmospheric dynamics, and as such provides a more complete accounting of the conservation properties of atmospheric flow (Shepherd 1993). Of special interest here is the depiction of horizontal propagation of wave activity afforded by Plumb's framework. Karoly et al. (1989) give some examples of this propagation for the Southern Hemisphere winter climatology and for several sta-

* Current affiliation: General Sciences Corporation, NASA/Goddard Space Flight Center, Greenbelt, Maryland.

Corresponding author address: Dr. William J. Gutowski, Atmospheric Science, Iowa State University, Department of Geological and Atmospheric Sciences, 3010 Agronomy Bldg., Ames, IA 50011-1010.

tionary anomalies such as the El Niño–Southern Oscillation and the Pacific/North American teleconnection patterns. They contend that the stationary wave activity flux is superior to geopotential height anomalies for determining the direction of wave propagation. Other studies have used the diagnostic for a variety of purposes. Black and Dole (1993) used the stationary wave activity flux as a tool to study the regional sources responsible for the development of atmospheric persistent anomaly patterns. Murphree et al. (1991) applied the diagnostic to understand the role of western Pacific tropical heating on the 1988 North American drought. Randel and Williamson (1990) computed the stationary wave activity flux for the season December–February as part of their comparison of operational analyses with the climate simulated by the Community Climate Model (Version 1) of the National Center for Atmospheric Research.

This paper is part of a series of papers that have compared GCM climate simulations of atmospheric dynamics as well as their change under CO₂ doubling. The focus here on stationary waves complements earlier studies of the zonal average zonal wind (Rosen and Gutowski 1992) and moisture and energy transports by transient eddies (Branscome and Gutowski 1992). Our purpose here is severalfold. One aim is to compare simulated versus observed stationary wave behavior, illustrating the strengths and weaknesses of GCM simulations produced by the Geophysical Fluid Dynamics Laboratory (GFDL) and the National Center for Atmospheric Research (NCAR). The two simulations analyzed have been used extensively to study potential societal impacts of a doubling of atmospheric CO₂ (i.e., regional climate change) and have archives containing data needed for the analysis here. We also examine seasonal variations in the stationary wave activity flux and, to a lesser extent, changes in the simulated flux under CO₂ doubling. Finally, we illustrate the usefulness of the stationary wave activity flux divergence for comparing *nondynamic* processes in models and the real atmosphere that may be difficult to observe directly.

2. Stationary wave activity

a. Flux

For stationary, quasigeostrophic disturbances about a steady zonal flow, Plumb (1985) derives the conservation relation

$$\frac{\partial A_s}{\partial t} + \nabla \cdot \mathbf{F}_s = C_s, \quad (2.1)$$

where A_s is a sum of the densities of wave activity and wave energy and \mathbf{F}_s is a measure of the flux of wave activity; C_s contains effects of nonconservative processes such as diabatic heating and (implicitly) topographic forcing and also higher-order products of dis-

turbance terms that arise from the disturbance's self-advection.

In spherical coordinates,

$$\mathbf{F}_s = \begin{Bmatrix} F_s^\lambda \\ F_s^\phi \\ F_s^z \end{Bmatrix} = \frac{p \cos \phi}{p_0} \times \begin{Bmatrix} v'^2 - \frac{1}{2\Omega a \sin 2\phi} \frac{\partial(v'\Phi')}{\partial \lambda} \\ -u'v' + \frac{1}{2\Omega a \sin 2\phi} \frac{\partial(u'\Phi')}{\partial \lambda} \\ \frac{2\Omega \sin \phi}{S} \left[v'T' - \frac{1}{2\Omega a \sin 2\phi} \frac{\partial(T'\Phi')}{\partial \lambda} \right] \end{Bmatrix}, \quad (2.2)$$

where (ϕ, λ, z) are the coordinates (latitude, longitude, $-H \ln \{p/p_0\}$); p is pressure; $p_0 = 1000$ mb; u' , v' , T' , and Φ' are the stationary disturbance's zonal wind, meridional wind, temperature, and geopotential height, respectively; and a and Ω are the earth's radius and rotation frequency, respectively. The quantity H is a scale height set equal to 7.5 km for all computations here. The term S is the static stability,

$$S = \frac{\partial \hat{T}}{\partial z} + \frac{\kappa \hat{T}}{H}, \quad (2.3)$$

where the caret denotes an areal average, and κ is the atmosphere's ratio of the gas constant R to the specific heat at constant pressure C_p . Areal averages here for computing S cover the region poleward of 20° latitude for the hemisphere under consideration.

Some important properties of this formulation relevant to the discussion here are (cf. Plumb 1985):

1) The term \mathbf{F}_s is a conserved measure of the flux of wave activity, appearing in a conservation relation, (2.1), relating $\nabla \cdot \mathbf{F}_s$ to nonconservative effects.

2) In the WKB limit of weakly dissipated, almost-plane waves, \mathbf{F}_s is phase independent and parallel to the group velocity.

3) The zonal average of \mathbf{F}_s is equal to the E–P flux of Edmon et al. (1980), aside from a zonal component that is inconsequential for zonally averaged dynamics.

4) In (2.2) \mathbf{F}_s involves calculation of first derivatives only, an advantageous feature for comparative diagnostic computations.

5) For steady waves, $\partial A_s / \partial t = 0$, and thus $C_s = \nabla \cdot \mathbf{F}_s$, allowing us to compare C_s in observations and simulations without computing it directly.

When we present figures of \mathbf{F}_s , we follow a plotting convention similar to that used by Edmon et al. (1980) for depicting E–P flux cross sections. Typically, we plot two components of \mathbf{F}_s as vectors on a surface such as a constant pressure level or a vertical cross section. On any surface, we require the vectors to look nondivergent

if and only if $\nabla \cdot \mathbf{F}_s = 0$. For our plotting units of degrees of latitude and longitude and meters of z on Cartesian grids, this requirement is satisfied by considering the product of $\nabla \cdot \mathbf{F}_s$ and the mass element dm in spherical log pressure coordinates:

$$dm = \frac{pa^2 \cos \phi}{gH} dz d\phi d\lambda, \quad (2.4)$$

where g is the gravitational acceleration. Then

$$\nabla \cdot \mathbf{F}_s dm = \left[\frac{\partial}{\partial \phi} (\cos \phi F_s^\phi) + \frac{\partial}{\partial \lambda} (F_s^\lambda) + \frac{\partial}{\partial z} (a \cos \phi F_s^z) \right] \frac{pa}{gH} dz d\phi d\lambda. \quad (2.5)$$

The term in brackets in (2.5) has the form of the divergence operator that one may apply mentally when observing vector plots on rectangular grids, so that plots of the vector

$$\tilde{\mathbf{F}}_s = (\cos \phi F_s^\phi, F_s^\lambda, a \cos \phi F_s^z) \quad (2.6)$$

will appear nondivergent on our plotting grids if and only if $\nabla \cdot \mathbf{F}_s = 0$. Our figures of stationary wave activity flux will use the plotting convention (2.6), but our discussion of the figures will be in terms of \mathbf{F}_s . Edmon et al. (1980) describe additional advantages of this plotting convention.

b. Source/sink

A shortcoming of property 5 above is that C_s is, of course, the sum of all nonconservative and wave self-advection effects, so that one cannot infer the influence of a particular process such as diabatic heating without additional information. While comparisons of simulated and observed C_s in themselves are still useful for assessing a model's simulation of the generation and dissipation of wave activity, the influence of diabatic heating alone is worth considering. For diabatic heating \mathcal{H} with stationary departures from the zonal mean \mathcal{H}' , the diabatic source/sink term for the stationary disturbance's quasigeostrophic potential vorticity q' is

$$s' = \frac{2\Omega \sin \phi}{p} \frac{\partial}{\partial z} \left(\frac{p \mathcal{H}'}{S} \right), \quad (2.7)$$

where \mathcal{H}' has dimensions degrees/time. Diabatic heating's contribution to C_s is then

$$C_{sd} = \frac{a \cos \phi}{(\partial Q / \partial \phi)} \frac{p}{2p_0} \left(q' s' - \frac{r'}{a \cos \phi} \frac{\partial}{\partial \lambda} q' \right), \quad (2.8)$$

where r' is defined by

$$\frac{1}{a \cos \phi} \frac{\partial r'}{\partial \lambda} = s' \quad (2.9)$$

and the requirement that r' vanish when integrated around a latitude circle. For wavelike distributions of s' in longitude, we have approximately

$$r' \propto \frac{-1}{a^2 \cos^2 \phi} \frac{\partial^2 r'}{\partial \lambda^2} = \frac{-1}{a \cos \phi} \frac{\partial s'}{\partial \lambda}, \quad (2.10)$$

so the second term in (2.8) is proportional to the longitudinal gradient of s' . Equations (2.7)–(2.8) also show that C_{sd} may be sensitive to the vertical distribution of diabatic heating.

As an illustration of the influence of diabatic heating on C_s , we have used output kindly supplied by the creators of a climatological, assimilation dataset under development (Schubert et al. 1993) that includes diabatic heating as well as the standard prognostic variables of the assimilating GCM. Data have been made available for the single month of January 1985, so these results do not constitute a climatology, but rather are indicative of the contribution of diabatic heating to C_s , a contribution we will not be able to compute directly from the climatological data we analyze later. Figure 1a shows the total diabatic heating at 700 mb in the northern extratropics, averaged over the month. Diabatic heating at other levels between 700 mb and the surface shows the same general pattern of positive maxima in the central Pacific and off the East Coast of North America and cooling elsewhere. The regions of strong positive heating appear to be induced by transient eddies in storm tracks (e.g., Chen and Baker 1986; Hoerling et al. 1990; Hoskins and Valdes 1990). In this example, the heating generally increases with height from the surface to the 700-mb level, so that s' in the lower troposphere (Fig. 1b) has positive maxima in the regions of maximum positive heating.

Figure 2a shows the vertical integral of C_{sd} between 1000 and 700 mb computed as

$$\begin{aligned} \int_{z(1000 \text{ mb})}^{z(700 \text{ mb})} C_{sd} dz &\sim C_{sd}(950 \text{ mb}) \\ &\times \{z(900 \text{ mb}) - z(1000 \text{ mb})\} + C_{sd}(850 \text{ mb}) \\ &\times \{z(700 \text{ mb}) - z(900 \text{ mb})\}. \end{aligned} \quad (2.11)$$

The diabatic source/sink for stationary wave activity, C_{sd} , is not simply proportional to the distribution of s' because, as seen in (2.8), C_{sd} involves the product of the heating with the dynamic field being forced, q' , as well as longitudinal gradients of s' and q' . For this month, extrema of q' (not shown) appear primarily over land, with the result that the largest magnitudes of C_{sd} also appear primarily over land. Several of the regions of strong C_{sd} arise from the r' term in (2.8), consistent with Plumb's (1985) suggestion that horizontal gradients of heating may play a significant role in determining the wave activity forcing. We will see later that $\nabla \cdot \mathbf{F}_s$ in the lower troposphere is dominated by its vertical derivative, suggesting a comparison here of C_{sd} with F_s^z emanating through the 700-mb level (Fig. 2b). For this comparison we use the vertical integral of (2.1) and assume that $F_s^z(1000 \text{ mb})$ lies below

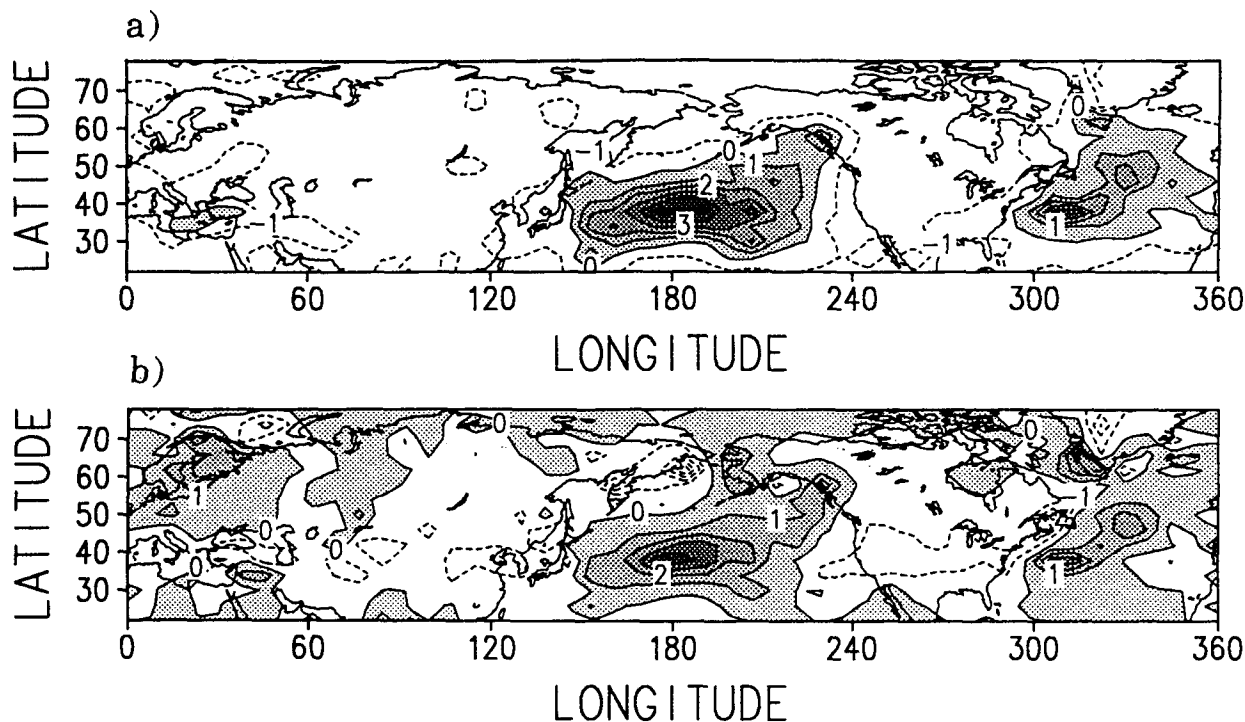


FIG. 1. (a) Diabatic heating at 700 mb and (b) s' from diabatic heating in the layer 950 mb–700 mb for the northern extratropics during January 1985. Contour intervals are (a) 1 K day^{-1} and (b) 10^{-10} s^{-2} .

the surface and hence equals 0. The strongest upward flux occurs in an area over northeastern China that is nearly coincident with one of the maxima in C_{sd} in the same region. Recalling our plotting convention, (2.6), in this region $F_s^z \sim 0.4 \text{ m}^2 \text{ s}^{-2}$, whereas vertically integrated $C_{sd} \sim 0.25 \text{ m}^2 \text{ s}^{-2}$, thus showing a significant role for diabatic forcing of stationary wave activity flux. For this region in particular, the dominant contribution to C_{sd} comes from the heating gradient term. Diabatic heating also gives a similar, substantial contribution to F_s^z over Newfoundland. Clearly, of course, the diabatic heating alone does not explain the entire distribution of F_s^z , although some of the differences between C_{sd} and $F_s^z(700 \text{ mb})$ may be due to our neglect of heating between 950 mb and the surface as well as to possible limitations in the analysis procedure yielding diabatic heating.

3. Models and data

The GCM output examined here comes from runs discussed by Washington and Meehl (1984; NCAR) and Manabe and Wetherald (1987; GFDL). The GCMs in both cases are spectral models that use zonal wavenumbers 0–15 in rhomboidal truncation for dynamical calculations and a 4.5° (latitude) \times 7.5° (longitude) grid for computing physical space processes. Model output is also archived on the $4.5^\circ \times 7.5^\circ$ grid. The models use nine layers for vertical finite differ-

encing, with the layers spaced unevenly to give highest resolution near the surface and tropopause. Each model includes realistic geography to within the accuracy of the horizontal resolution and a slab ocean whose thermal inertia allows the model to simulate an annual cycle of surface temperature. Neither model's ocean transports heat horizontally. In addition, each model includes a hydrological cycle and internally computed cloud cover, snow cover, and sea ice. Schlesinger and Mitchell (1987) give a detailed comparative description of the models. Models with finer horizontal resolution have been used to simulate effects of doubling atmospheric CO_2 , but based on results of the analysis, we will contend that improving stationary wave simulations and their change under CO_2 doubling depends strongly on improving our ability to model certain key physical processes. Results of the present study thus should not be altered by including output from models of higher resolution.

Two important factors for the forcing of atmospheric stationary waves are topography and land–ocean distribution. Because the models have the same horizontal resolution, their resolved land–ocean distributions are similar, although related factors such as surface–atmosphere heat exchange may differ (Gutowski et al. 1991). Despite having the same resolution, however, their topographic heights differ substantially (Fig. 3). The NCAR model uses Pitcher et al.'s (1983) spectral coefficients of topography, which were computed from

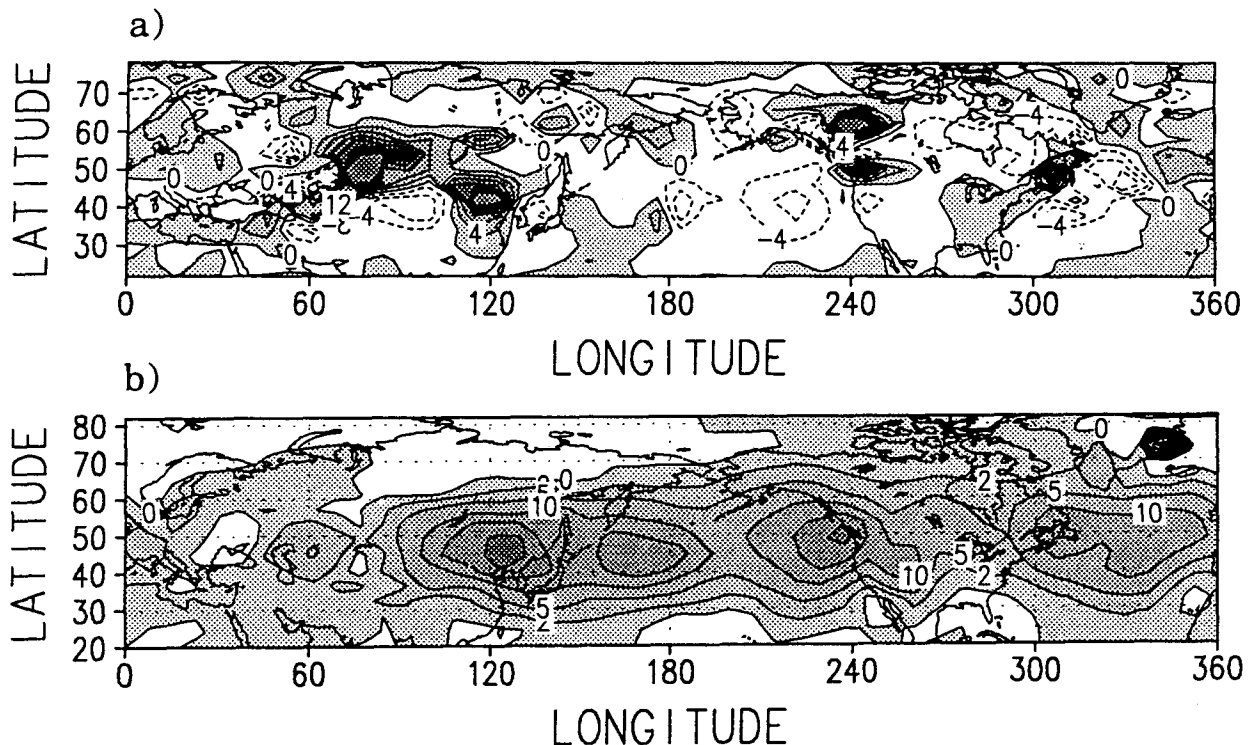


FIG. 2. (a) Vertical integral of C_{sd} between 1000 and 700 mb for January 1985. Contour interval is every $4 \times 10^{-2} \text{ m}^2 \text{ s}^{-2}$ up to $24 \times 10^{-2} \text{ m}^2 \text{ s}^{-2}$. (b) F_2^2 at 700 mb for the northern extratropics during January 1985. Contours are at 0, 2, 5, 10, 15, and 20 ($\times 10^5 \text{ m}^3 \text{ s}^{-2}$). In both panels, positive values are shaded.

a spatially smoothed grid point dataset. The GFDL model's coefficients, on the other hand, were computed without prior smoothing of the input gridpoint data (Broccoli 1990, personal communication). The models also differ in their treatments of clouds, radiation, and details of condensation parameterizations, processes that can influence the generation and dissipation of wave activity. Subgrid-scale momentum exchange between the surface and the atmosphere can further alter wave activity. Both models compute this momentum flux using a drag law for which the drag coefficient C_D assumes a constant, relatively low value over the ocean and a relatively high value over land. Finally, the models apply a diffusion operator that acts as a wave activity sink by simulating (crudely) enstrophy cascade beyond the truncation limit. The diffusion is scale selective, however, and has negligible influence on synoptic and larger scale waves.

For each model, we analyze output from two runs: a control run with current levels of atmospheric CO_2 and a climate perturbation run using doubled CO_2 . We compute stationary wave statistics using archived output averaged over the final 10 years of the GFDL model run and the final 3 years of the NCAR model run. Our analysis focuses on output for two seasons: December–January–February (DJF) and June–July–August (JJA). Making use of the hydrostatic relation,

we use each model's surface heights and time-averaged temperature fields to obtain distributions of geopotential height as a function of model layer. We then interpolate the height fields vertically to the pressure levels of our observational dataset (below) and compute necessary stationary wave data for (2.2) using the geostrophic and hydrostatic relations.

The observational data in this study come from the Climate Diagnostics Data Base of the National Meteorological Center (NMC). The data are archived on a 2.5° latitude–longitude grid at the pressure levels 1000, 850, 700, 500, 300, 250, 200, 100, and 50 mb. We use the database's monthly mean values of temperature and geopotential height for the period October 1978–March 1990, which we combine into a 12-yr DJF average and an 11-yr JJA average. As with the model output, we compute data for (2.2) by applying the hydrostatic and geostrophic relations to the stationary wave height fields. Although the NMC data is available on a $2.5^\circ \times 2.5^\circ$ grid, we only use data every 5° (lat) $\times 7.5^\circ$ (long) to conform more closely with the grids of the model data. Note that we do not pass the observational data through a filter that truncates the data at the spectral resolution of the models. Stationary wave energy and enstrophy spectra, however, are dominated by synoptic and planetary scales (Boer and Shepherd 1983), so any spectral modes in the NMC data that

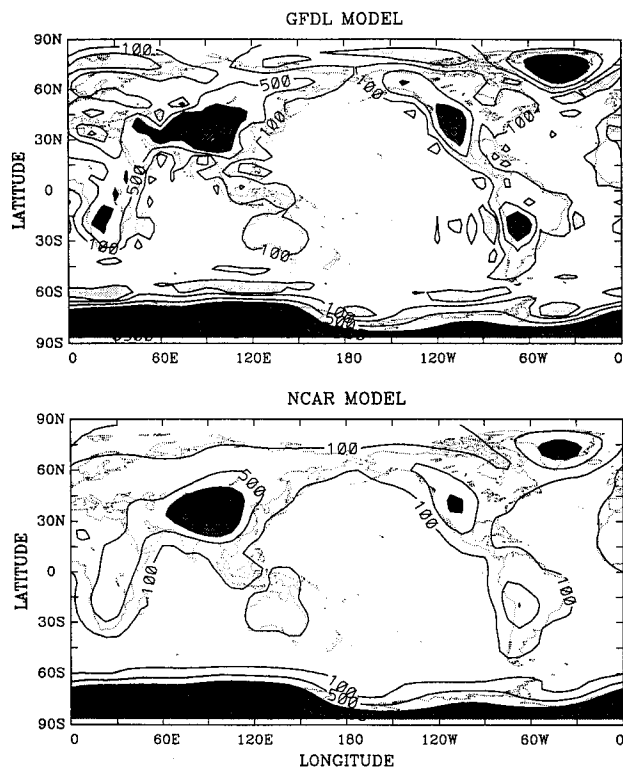


FIG. 3. Surface heights for the GFDL model (upper panel) and the NCAR model (lower panel). Contours are at -100 , $+100$, 500 , 1000 , 1500 , ... m. Heavy shading: height > 1000 m; light shading: height < -100 m.

fall outside the models' truncation limits should be of negligible importance for the comparisons here.

The observational data is a product of the NMC data assimilation cycle, and the quality of the observational statistics may therefore be influenced by the accuracy of NMC's assimilation scheme as well as its evolution with time. Trenberth and Olson (1988) have documented the reliability of NMC analyses and performed an assessment of their accuracy, in part through comparison with analyses produced by the European Centre for Medium-Range Weather Forecasts (ECMWF) for the years 1980–1986. They find that in the Northern Hemisphere extratropics, the rotational wind and geopotential height and temperature fields should be reasonably well known. In the Southern Hemisphere extratropics, however, the accuracy of geopotential height analyses, and hence all quasi-geostrophic quantities, decreases with increasing latitude, becoming especially poor over Antarctica.

Trenberth and Olson (1988) assess the accuracy of the NMC Southern Hemisphere analyses in part by computing rms differences between the NMC and ECMWF analyses. For comparison, we measure the amplitude of stationary waves in our observational dataset by the magnitude of their standard deviation in geopotential height about a latitude circle, a quantity

(not shown) that decreases toward the South Pole from a maximum in the zone 50°S – 60°S . Poleward of roughly 65°S , the amplitude of the stationary waves becomes smaller than the NMC–ECMWF rms differences, indicating that any quasigeostrophic analysis based on these waves should be restricted to extratropical latitudes north of 65°S . Even within the region 20°S – 65°S , the stationary wave amplitude exceeds the NMC–ECMWF rms differences by, at most, a factor of 2. While the NMC–ECMWF differences are not restricted to differences in stationary waves alone, the comparison does suggest limited accuracy for the observational, Southern Hemisphere stationary wave data.

4. Observation–model comparison

We first compare patterns of F_s from the control runs of the GFDL and NCAR models with those computed from the NMC analyses. Our principal focus is the period and domain that has the strongest stationary waves, Northern Hemisphere DJF (e.g., Oort 1983). Many of our depictions of F_s show the horizontal components at 300 mb and the vertical component at 850 mb. Examination of F_s at several levels shows that the specific levels used are not critical for revealing features of the wave activity flux so long as the horizontal components are shown for an upper-tropospheric level and the vertical component is shown for a lower-tropospheric level. The behavior of the horizontal component is consistent with the equivalent barotropic structure typically observed for quasi-stationary waves in the atmosphere (Blackmon et al. 1979; Hoskins and Karoly 1981; Wallace and Gutzler 1981).

a. Northern Hemisphere DJF

Before comparing observed and simulated F_s , it is useful to compare the NMC values computed here (Fig. 4) with earlier depictions. Plumb (1985) used daily NMC analyses from 1965 to 1975 to compute F_s for a 120-day season beginning on 15 November. In general, the major features of both computations are the same. Over most of the northern extratropics in each dataset the stationary wave activity propagates upward and eastward, emanating primarily from three regions: eastern Asia, the eastern Pacific, and the northern Atlantic. Also in both datasets, F_s south of 50°N tends to be directed equatorward whereas F_s north of this latitude tends to be directed poleward. As noted by Plumb (1985), the splitting of F_s over eastern Asia into poleward and equatorward branches is consistent with Rossby wave ray tracing (cf. Hoskins and Karoly 1981; Webster 1981; Webster 1982). Similar general characteristics for F_s also appear in ECMWF operational analyses averaged over 1980–1986 (Randel and Williamson 1990). Finally, recalling that the zonal average of the meridional and vertical components of F_s

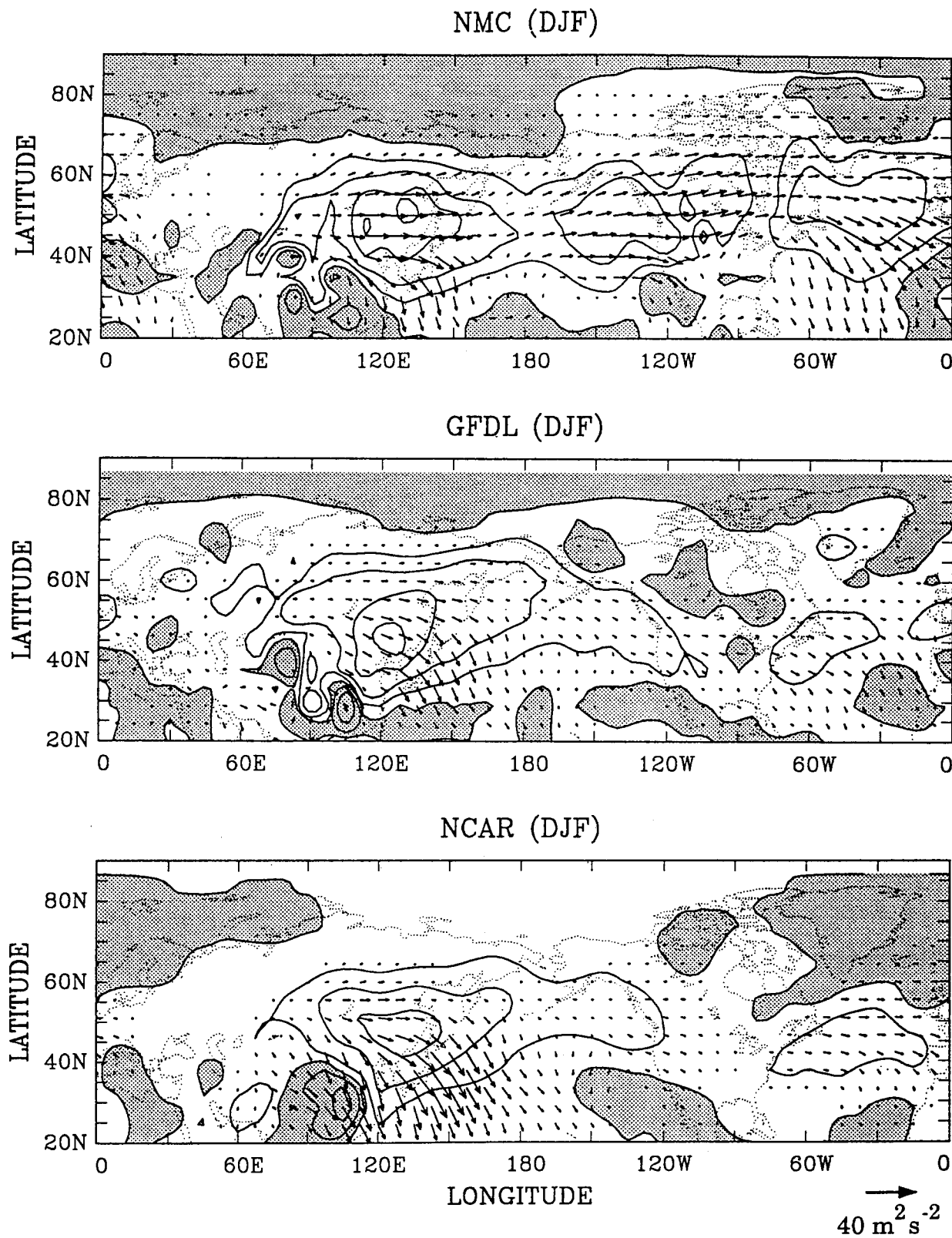


FIG. 4. Components of \mathbf{F} , for Northern Hemisphere DJF from NMC analyses and control climates of the GFDL and NCAR models. Vectors are the 300-mb horizontal components (in $\text{m}^2 \text{s}^{-2}$), with a scale at the lower right. Contours are the 850-mb vertical component, with contours at $-10, -5, -2, 0, 2, 5, 10$, and $15 (\times 10^5 \text{ m}^3 \text{s}^{-2})$. Negative values are shaded.

reduce to the E-P flux, the behavior of F_s in Fig. 4 is also consistent with the winter, Northern Hemisphere E-P flux computed by Edmon et al. (1980) from observations.

Some notable differences also appear between the flux depictions here and in Plumb (1985). Horizontal wave train propagation over western North America and the subtropical Atlantic is stronger in the later dataset, so that the relative strengths of F_s in the three emanation regions are more alike in the later data than in the earlier data. In contrast, vertical fluxes over eastern Asia are somewhat stronger in Plumb's dataset. Also, at longitudes 180° , 100°W and 40°E in the more recent but not the earlier data, there appears to be support for the suggestion of Held (1983) that equatorward-propagating wave trains might be reflected poleward from critical latitudes in the tropics. [Similar evidence for reflection appears in 1980–86 ECMWF data (Randel and Williamson 1990, Fig. 18).] These differences may represent changes in "stationary" waves from one decade to another, or they may be the result of the many changes in the NMC analysis scheme over the period 1965–1990. Distinguishing between these two factors is not possible here, but these differences do place a limit on how precisely we can fix F_s .

The model simulations (Fig. 4) also show a three-branch structure with eastward propagation. The models are most successful in simulating the strong East Asian source of F_s and the subsequent propagation of the flux toward the subtropics. The NCAR model does especially well in simulating the magnitude of the vertical component, whereas the GFDL simulation compares favorably with observations in its depiction of the equatorward propagation in this region. The models, however, show substantially weaker F_s than observed over the eastern Pacific and North Atlantic. The largest disparities between Plumb's (1985) and our observational F_s also occur in these regions, suggesting a greater sensitivity of F_s here to variations in the general circulation, whether real or the product of analysis scheme changes. The sensitivity might make the simulation of stationary wave activity more difficult in these regions. The observation–model differences are greater than those between the two sets of observations, however. The models also fail to reproduce much, if any, of the poleward propagation seen in the observed F_s north of 50°N .

Vertical cross sections at selected latitudes and longitudes (Figs. 5–7) further confirm behavior discussed above as well as show its continuity through the depth of the troposphere. The midlatitude longitude–height section in Fig. 5 is near the maximum vertical propagation in each of the three branches of strong F_s . For both the models and the observations, wave activity propagates upward and eastward from surface sources. The models sustain neither upward nor eastward propagation as well as the observed flow does. Especially noticeable is the models' convergence of F_s in the lower

troposphere over eastern Asia (120°E), revealing a net sink of wave activity present in the models that does not occur in the atmosphere. The sink may represent a difference in physical behavior between the atmosphere and the models. Or, because the models represent the entire depth of the atmosphere with just nine layers, vertical finite differencing may create a numerical sink in the models. Also in Fig. 5 is an upper-level source of F_s at 120°E in the NCAR model that does not appear in the other two datasets.

A latitude–height cross section along 120°E (Fig. 6) shows again the more rapid decrease of F_s with height in the models compared to the atmosphere. Figures 5 and 6 together show that the decrease is truly due to a net sink and not simply to a turning of the flux out of the plane depicted in either figure. In addition, Fig. 6 shows the continuity of the wave activity propagation, first vertically and then laterally from the surface source, with very little poleward propagation in the simulations. Finally, the figure also shows the NCAR simulation's upper-level source.

A latitude–height cross section over the central Pacific (Fig. 7) shows rather different behavior in the observations compared to the cross-section over eastern Asia. Here, stationary wave activity propagates poleward from the subtropics to merge with the upward flux in midlatitudes. The source of this flux may reside farther south. As noted above, however, the poleward F_s in the subtropics may also be caused by stationary waves that transport energy equatorward before being reflected poleward at critical latitudes. Figure 7 shows that poleward flux occurs at all levels in the observed subtropics, consistent with the equivalent barotropic structure anticipated for reflecting stationary waves (Held 1983). No propagation from the subtropics occurs in the models, revealing a substantial difference between the models and the observed atmosphere in their stationary waveguides for this region. The figure also indicates midlatitude, interior sources of wave activity in the lower troposphere of the observed atmosphere and the upper troposphere of the NCAR model.

The model simulations of F_s are much closer to each other than to the observed flux. Both models have spectrally truncated topography, which will tend to reduce topographic heights and perhaps reduce forcing of stationary waves. Sensitivity to topography may be evident in that the GFDL model produces a stronger upward flux over eastern Asia than the NCAR model, which has lower topographic heights in the vicinity of the Tibetan plateau (Fig. 3). Although topographic forcing appears to play a role in generating F_s over eastern Asia (Plumb 1985), the models' wave activity fluxes are comparable in magnitude to the observed despite the smoothed topography. In contrast, the simulations' weak upward fluxes over western North America may be a consequence of the smoothing. The North Atlantic F_s , on the other hand, is generated far from major mountain chains, and so its relatively weak

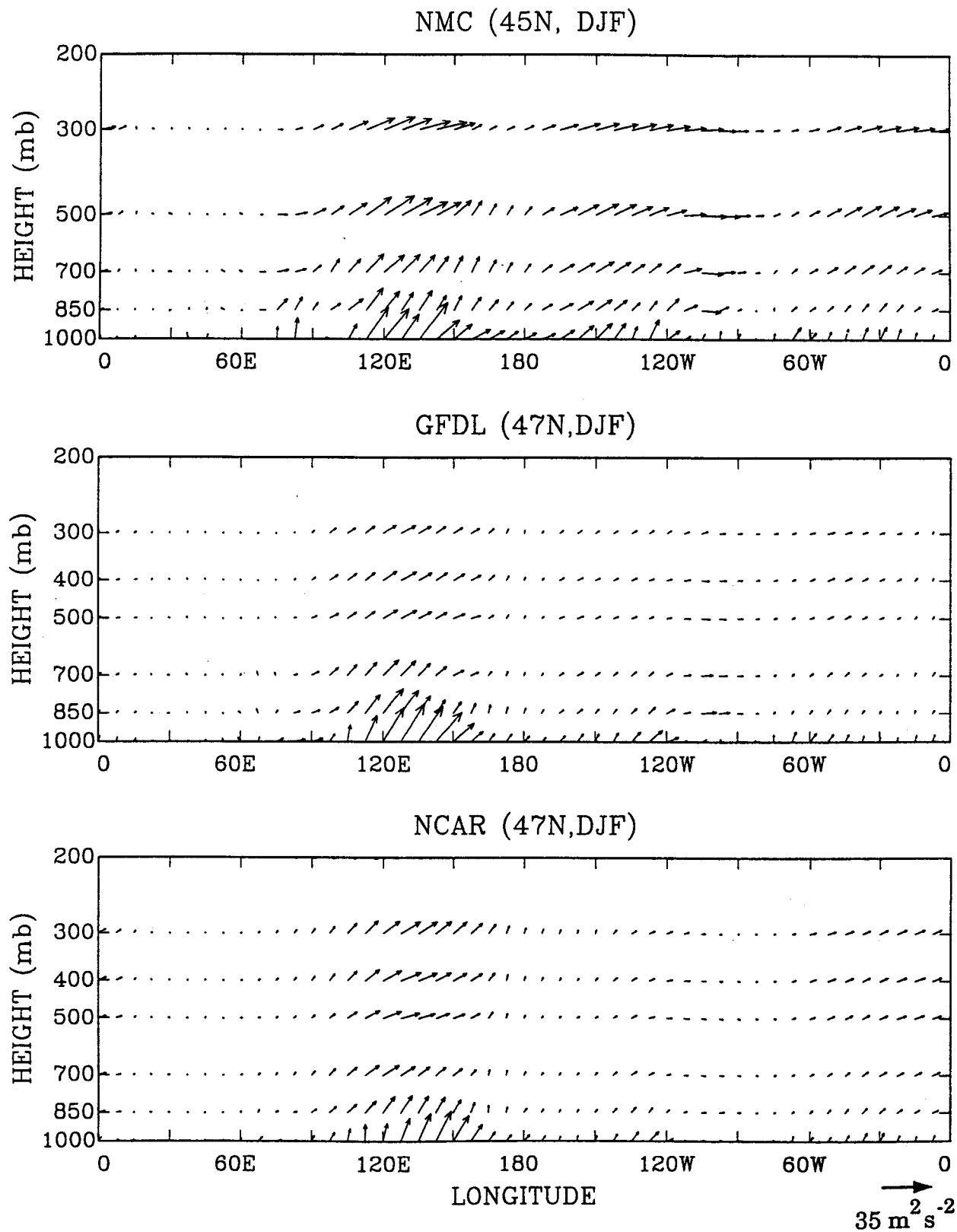


FIG. 5. Longitude-height sections of DJF F_2 along 45°N for the observed atmosphere (NMC) and along 47°N for the simulated climates (GFDL and NCAR). Units are $\text{m}^2 \text{ s}^{-2}$, with values of the vertical component multiplied by 10^{-5} before plotting.

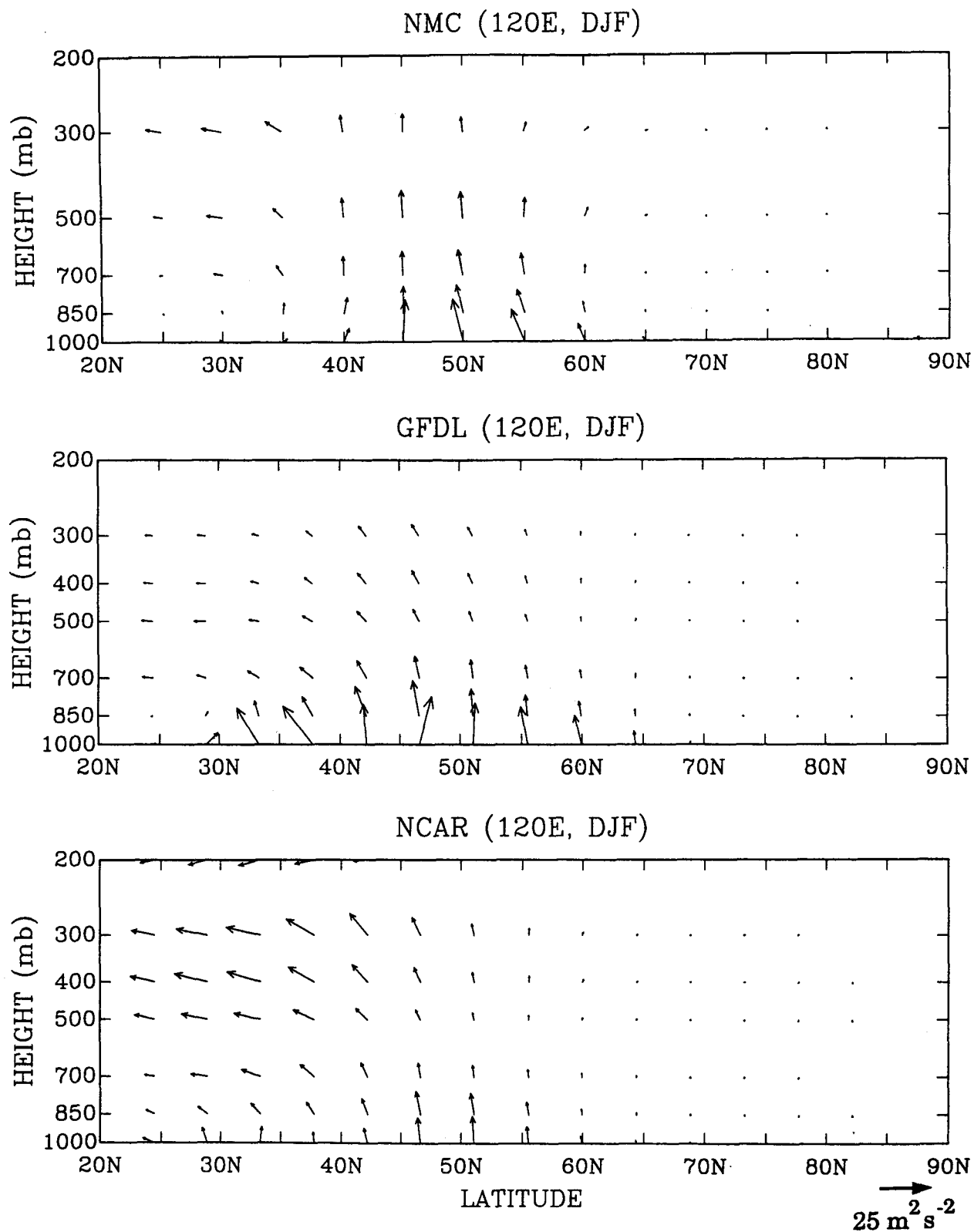


FIG. 6. As in Fig. 5 but for latitude-height sections along 120°E.

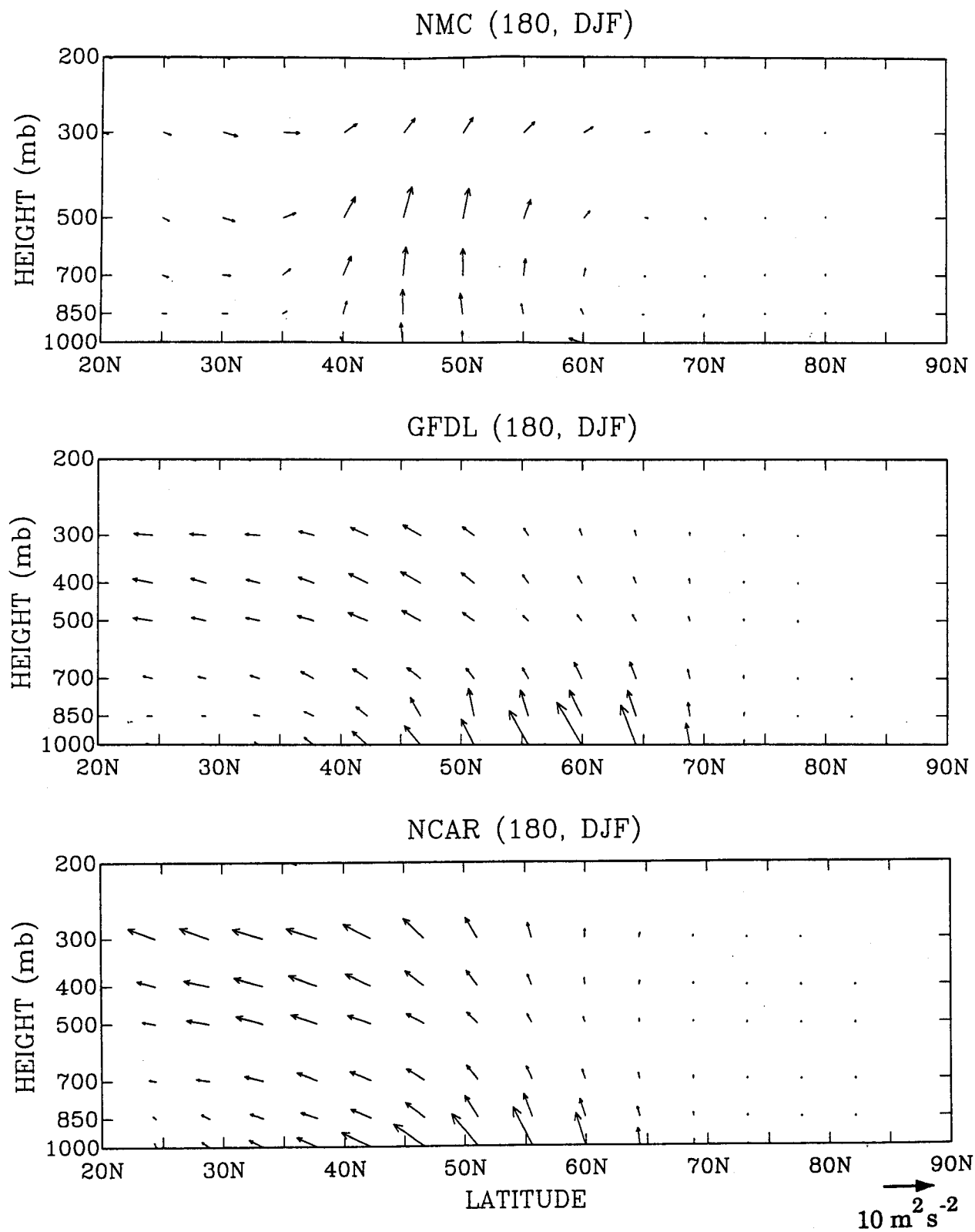


FIG. 7. As in Fig. 5 but for latitude–height sections along 180°.

simulation may have little to do with the models' representations of topography.

If topographic generation of F_s is deficient over East Asia, then other types of generation in the models must be larger than in the real atmosphere. Figure 2 shows that diabatic heating in the atmosphere may contribute to the generation in this region. Both models have DJF precipitation rates over the North Pacific that are larger than observed (Schlesinger and Mitchell 1987), a behavior that would yield larger s' and $\partial s'/\partial \lambda$ over East Asia if the vertical distribution of condensation is similar to that of the real atmosphere. The models, however, also have larger than observed precipitation rates in the North Atlantic, where F_s is weaker than observed. Transient waves can also affect the stationary wave activity, either by direct dynamical interaction (Plumb 1985, 1986) or by stimulating latent heat release. Dynamical interaction may be important for generating stationary wave activity in all three major branches of the stationary wave activity flux, and it may produce the upper-level source of stationary wave activity seen in the NCAR model (Figs. 5–7). Insufficient data are available from the present models to determine the influence of transient waves on the simulated F_s .

Finally, as noted earlier, the waveguide for stationary waves poleward of 50°N appears to be markedly different between the simulations and the observations. Differences in low-level sources would not appear to be a direct cause of the behavior, since there is more upward propagation over extreme northeastern Asia in the models than in the observations, nor do the differences appear to be related to interactions with transient eddies, since much of the poleward propagation occurs outside the primary storm track regions off the east coasts of Asia and North America.

b. Northern Hemisphere JJA

The JJA F_s (Fig. 8) shows marked changes from its distribution during DJF. The JJA horizontal flux is much weaker, consistent with the observed seasonal cycle of Northern Hemisphere standing waves (Oort 1983). The three-branch structure seen in DJF is not apparent in JJA, though there are regions of maximum upward flux at 850 mb over the eastern Pacific and the North Atlantic. In the models, the magnitudes of these flux maxima are actually stronger than the corresponding DJF maxima. In addition, for all three datasets, the maxima in JJA appear to be shifted equatorward from their DJF locations. This is in contrast with the more typical poleward shift in summer for dynamical quantities, although the JJA maxima may be caused by different phenomena than those producing the DJF maxima, and therefore may not necessarily represent an equatorward shift. Finally, both the models and the observed flow have substantial wave activity flux in the region of the summer monsoon over India and Southeast Asia, though one may question whether

or not any of the datasets have sufficient resolution to adequately resolve stationary wave dynamics associated with the summer monsoon.

Perhaps the most intriguing difference between DJF and JJA F_s is the predominantly downward 850-mb flux during the latter season. Again recalling the correspondence between zonal average F_s and the E–P flux, Edmon et al. (1980) find a similar behavior in their E–P flux analyses for Northern Hemisphere summer. The continued appearance of downward flux in a later, and presumably more accurate, atmospheric dataset indicates that the phenomenon is indeed real. The appearance of downward flux in the models indicates that they also contain the physics causing the behavior. This last result is important for, as Edmon et al. (1980) note, typical linear models of orographically and thermally forced stationary waves do not yield downward wave activity flux. The model results suggest that the responsible forcing arises from known processes and not some hitherto unrecognized physics.

Edmon et al. (1980) consider two possible causes for downward wave activity flux: nonlinear interaction with transient waves and convection. The longitudinal resolution of wave activity flux afforded by the F_s analysis here indicates only weak forcing from interaction with transient waves, for there is very little concentration of the downward flux in the JJA storm track regions over the North Atlantic and North Pacific (cf. Lau et al. 1981). Convection, on the other hand, may play a more substantial role, because as noted earlier, the wave activity forcing in (2.1), C_s , includes a term proportional to the vertical derivative of diabatic heating; thus, it may be sensitive to differences in convective heating between the models and the atmosphere. A contribution by summertime, extratropical convection to upper-tropospheric forcing of stationary waves is also implied by Kang and Held's (1986) study of stationary wave responses to a GCM's field of velocity potential. Both models here simulate convection by moist-adiabatic adjustment, which does not produce deep, penetrating convection. As a consequence, the models' vertical distributions of time-average convective heating, and hence their diabatic forcing of stationary wave activity, should be skewed toward the surface relative to the atmosphere's distribution. This behavior is consistent with cross sections of the simulated and observed F_s , such as the latitude–height section along 150°E (Fig. 9). Furthermore, the minimum relative humidity for convection is lower in the NCAR model (80%) than in the GFDL model (100%), which may cause convection to occur more readily in the NCAR simulation, giving more convective heating on average. In Fig. 9, the NCAR model's stronger downward flux compared to that of the GFDL model is consistent with an assumption of stronger time-average convective heating in the NCAR model.

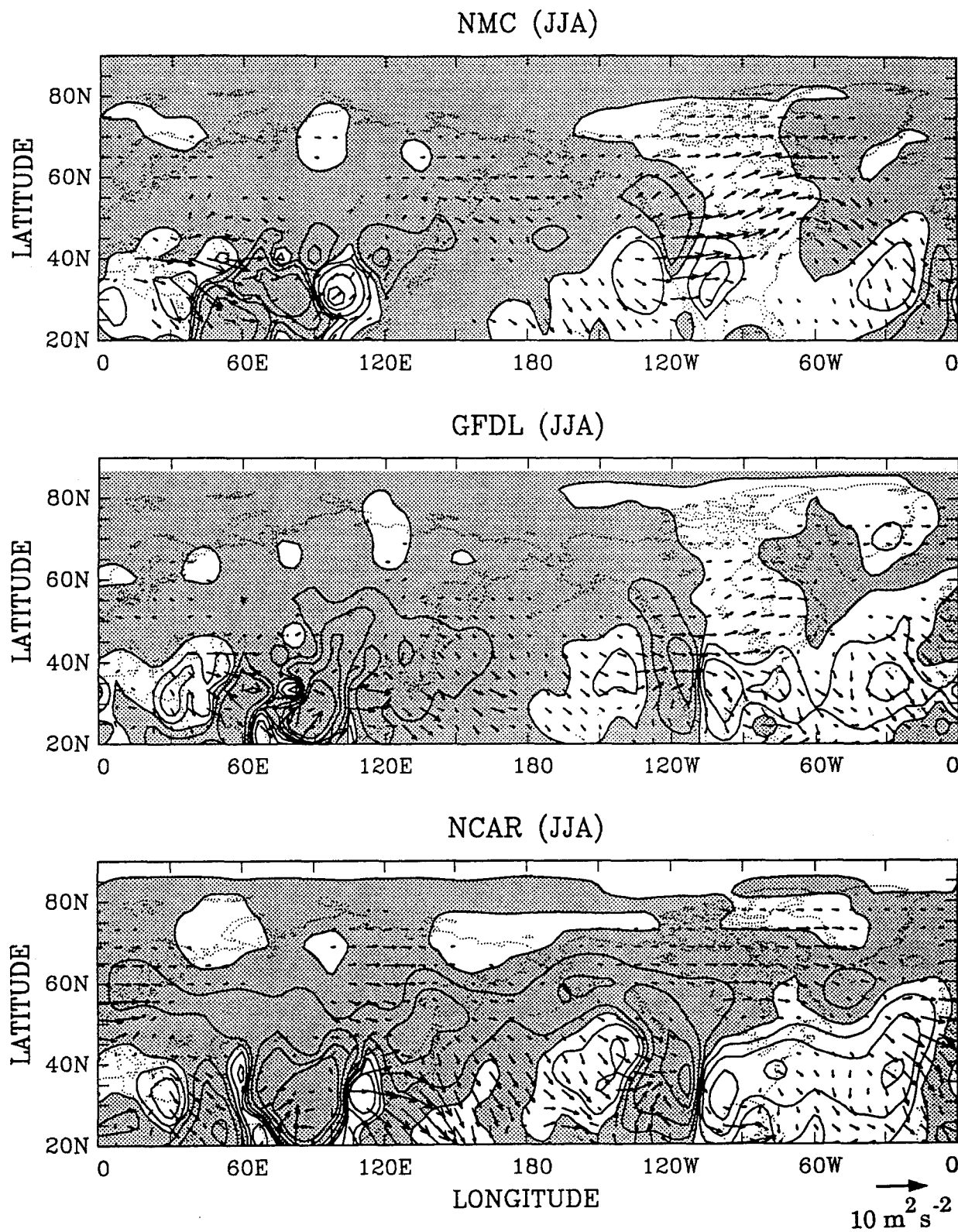
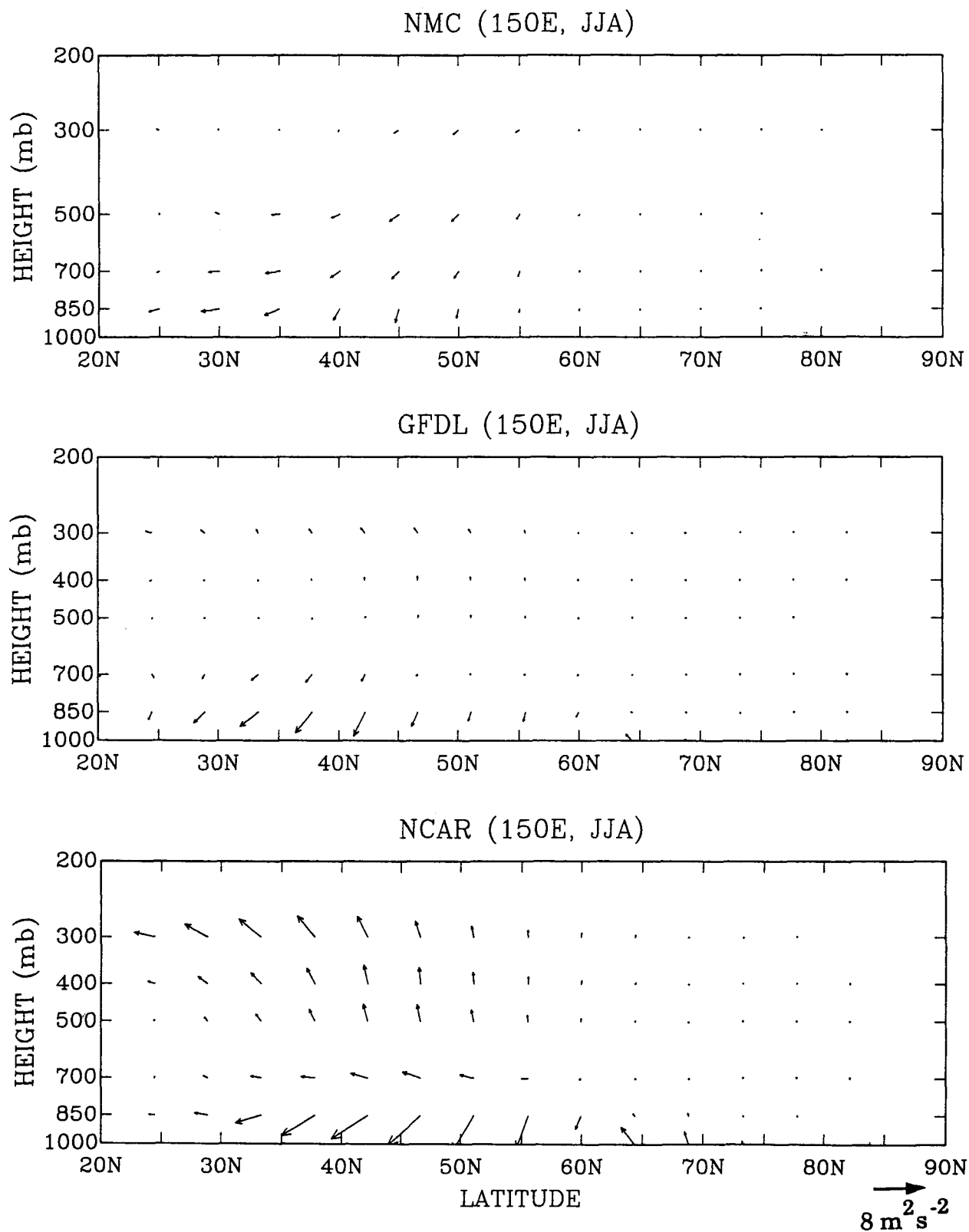


FIG. 8. As in Fig. 4 but for Northern Hemisphere JJA. Vectors are the 300-mb horizontal component (scale at lower right), contours are the 850-mb vertical component.

FIG. 9. As in Fig. 5 but for JJA latitude-height sections of F_s along 150°E .

c. Southern Hemisphere

In the Southern Hemisphere extratropics, there are no stationary centers of strong planetary wave forcing such as high, broad mountains, regions of intense diabatic heating, or storm tracks highly confined in longitude. Thus, compared with the Northern Hemisphere DJF, stationary waves in the Southern Hemisphere are weaker (Oort 1983). Furthermore, as discussed earlier, our confidence in the quality of Southern Hemisphere observational data is limited, so our discussion of F_s in the Southern Hemisphere will not be as extensive as it is for the Northern Hemisphere.

Despite the relative weakness of the Southern Hemisphere F_s and the uncertainties in Southern Hemisphere stationary wave observations, there is fairly good agreement between the NMC JJA flux (Fig. 10) and the JJA flux computed by Karoly et al. (1989) using Australian Bureau of Meteorology analyses for 1972–1982. Both datasets show that the strongest 300-mb F_s emanates from the central Indian Ocean to pass south of Australia and then northward into the central Pacific. The source region for F_s coincides with a zone of substantial convergence of transient wave activity (Trenberth 1991), supporting Karoly et al.'s (1989) suggestion that the stationary wave activity here is forced by nonlinear interaction with transient waves in the principal Southern Hemisphere storm track. Consistent with such interaction, a latitude–height cross section along 90°E (Fig. 11, upper panel) shows a source of F_s near 40°S that extends through the troposphere, indicating internal, barotropic forcing. Even stronger forcing appears in this cross section's lower atmosphere, near 65°S, but as discussed earlier, the accuracy of stationary wave observations this far south is poor, so the significance of this forcing is uncertain.

Both datasets also show relatively large wave activity flux emanating near Antarctica toward southern Africa. In this instance, the source of the flux appears to be at the surface near 60°S (Fig. 11, lower panel). The source region is near Antarctica's highest surface elevations, so the flux may represent the northward-propagating, topographically forced stationary waves studied by Watterson and James (1992) using numerical models of an idealized Antarctic continent, though their wave trains suggest more westward propagation than appears here [cf. F_s and corresponding wave train plots in Plumb (1985) and Karoly et al. (1989)]. The source region, however, is also near the JJA ice line, where there could be a large gradient in the strength of surface heat exchange with the atmosphere, potentially yielding significant diabatic forcing of stationary wave activity. Figure 10 shows an additional source for this flux in the vicinity of the Drake Passage. Sea surface temperature difference between the Atlantic and Pacific Oceans may be responsible for this source (van Loon and Jenne 1972), although its importance is uncertain

because it is not as prominent in the Karoly et al. (1989) analysis.

The models have difficulty simulating both the strength and the direction of stationary wave activity flux in the Southern Hemisphere (Fig. 10). The GFDL model has virtually no standing wave flux, whereas the NCAR model does simulate a flux from the Indian Ocean to a region south of Australia, although this flux is weaker in the NCAR model than in the NMC dataset. From the discussion above, model simulations of F_s in the Southern Hemisphere would appear to depend critically on their simulations of transient eddies in the upper troposphere. Malone et al. (1984) have studied eddy simulations in a version of the NCAR model that is similar to the one examined here but with specified sea surface temperatures in perpetual-month simulations. In their version, July transient eddies in the Southern Hemisphere's upper troposphere are roughly 10%–20% weaker than observed. Comparable results from the GFDL model are not available, though Manabe and Hahn's (1981) limited Southern Hemisphere analyses of a GFDL model run with specified, seasonally varying sea surface temperatures hints at a similar weakness in the GFDL model's transient eddies.

Neither model exhibits a northward flux of stationary wave activity toward Africa. Both do simulate relatively large gradients in surface–atmosphere heat exchange near Antarctica (Gutowski et al. 1991), so they do not appear to lack sufficient diabatic forcing. In fact, because neither model's sea ice includes leads, their atmospheric heating gradients between ice-covered and open-ocean areas are likely to be too strong compared to actual gradients (Mitchell and Senior 1989). The models' spectral truncations may smooth the topography and weaken stationary wave forcing, but Watterson and James (1992) have no trouble obtaining topographically generated stationary waves using a fairly modest, idealized mountain to represent Antarctica. Furthermore, although Held and Ting (1990) have shown that the irregularly spaced sigma-coordinate grids used by these models may distort stationary wave forcing, the error induced should produce waves that are too strong rather than too weak. Thus the absence in these models of stationary wave activity flux emanating from Antarctica is puzzling. The simulation of stationary waves near Antarctica may be sensitive to the models' simulations of low-frequency transient waves (Watterson and James 1992), which results in Malone et al. (1984) and Manabe and Hahn (1981) indicate may be too weak in the Southern Hemisphere. In addition, the models have difficulty matching the observed distribution of easterlies and westerlies in this region (Rosen and Gutowski 1992), which may further alter their forcing of stationary waves near Antarctica.

The observed DJF F_s in the Southern Hemisphere (Fig. 12) shows a slightly weaker but otherwise similar pattern compared to the JJA F_s , consistent with the small seasonal variability observed in extratropical,

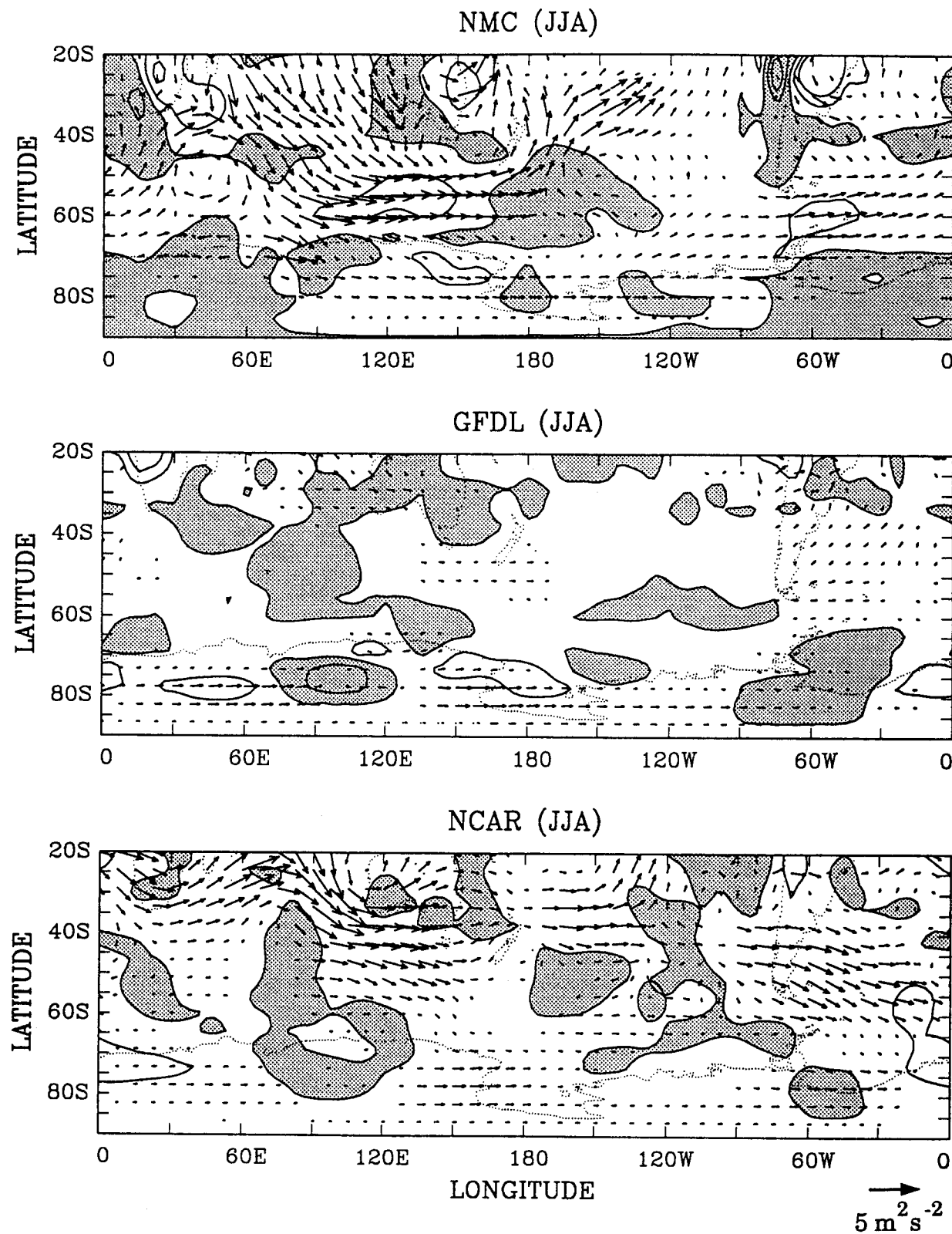


FIG. 10. As in Fig. 4 but for Southern Hemisphere JJA. Vectors are the 300-mb horizontal component (scale at lower right); contours are the 850-mb vertical component. Contours are at $-5, -2, -1, 0, 1, 2$, and $5 (\times 10^3 \text{ m}^2 \text{ s}^{-2})$.

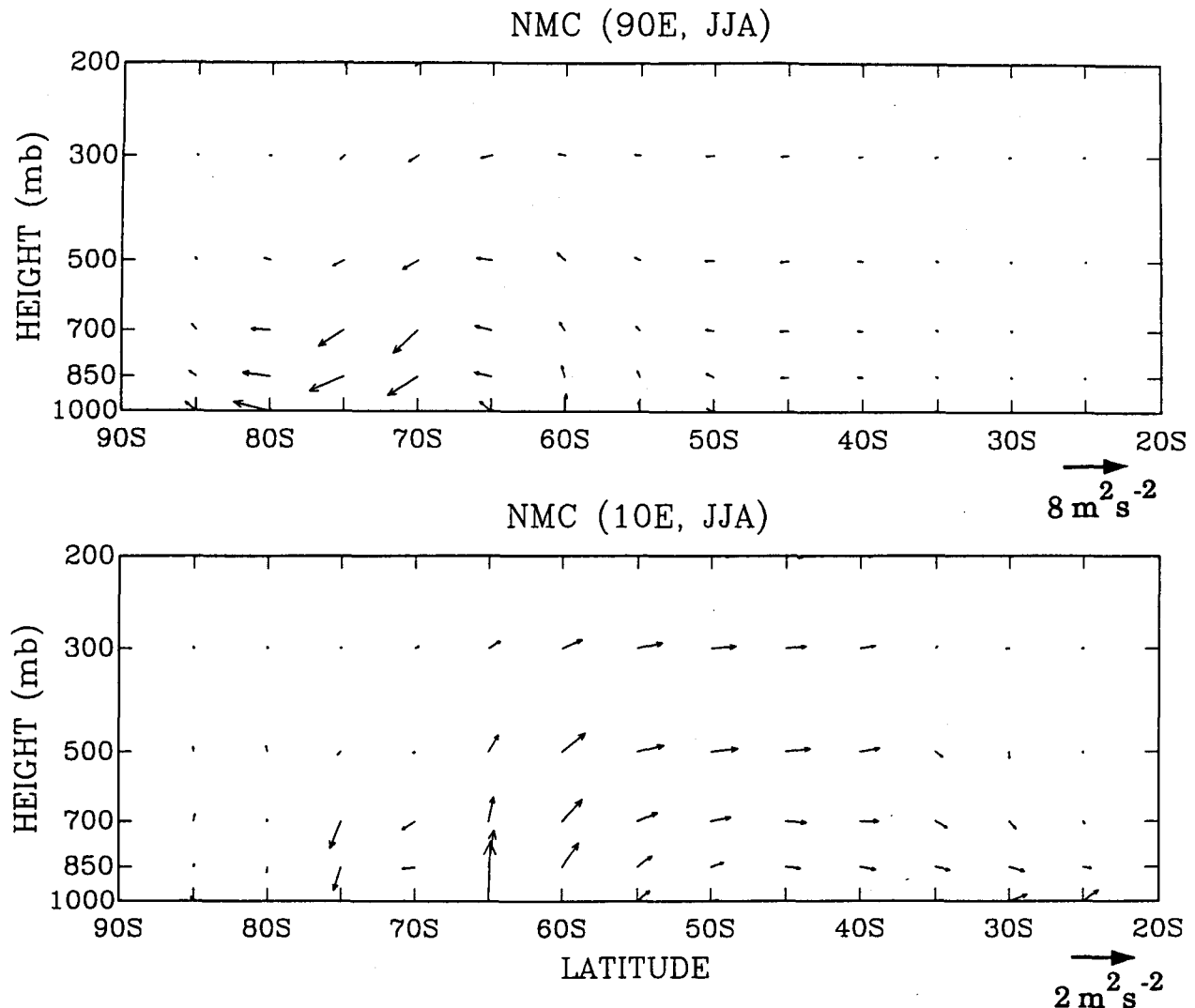


FIG. 11. Southern Hemisphere latitude–height sections of JJA F_s from the observed (NMC) climate along 90°E (upper panel) and 10°E (lower panel). Plotting conventions are the same as Fig. 5; note the different vector scales for each panel.

Southern Hemisphere dynamics (Oort 1983; Trenberth 1991). The models again reproduce fairly poorly the observed horizontal flux, though they do have some success in simulating the dipole patterns in 850-mb vertical flux over Australia and South America.

5. Discussion and summary

As noted earlier, these two models have been used extensively to study potential impacts of CO₂ doubling. Because stationary wave changes could affect regional climate and thus societal impacts of potential global warming, a consideration of CO₂-doubling changes in stationary wave activity is warranted. The models' changes in F_s under CO₂ doubling (not shown) are roughly one-quarter the magnitude of the strongest wave activity fluxes in the control climates, a change

that could be substantial. The flux changes show little consistency between the two models, however, so little confidence can be ascribed to the projected changes in stationary waves. For this reason, no further analysis of CO₂-doubling changes is presented here. The inconsistency represents a severe shortcoming in the models' simulations of regional climate change. Most likely, changes in the horizontal propagation of stationary wave activity are tightly linked to the changes in the upper troposphere's zonal mean circulation, changes for which these models show little agreement (Rosen and Gutowski 1992).

For the current climate, however, F_s computed from different observational datasets shows a number of robust features of stationary waves in both the Northern and Southern Hemispheres that the models should simulate. Consistent with well-known characteristics

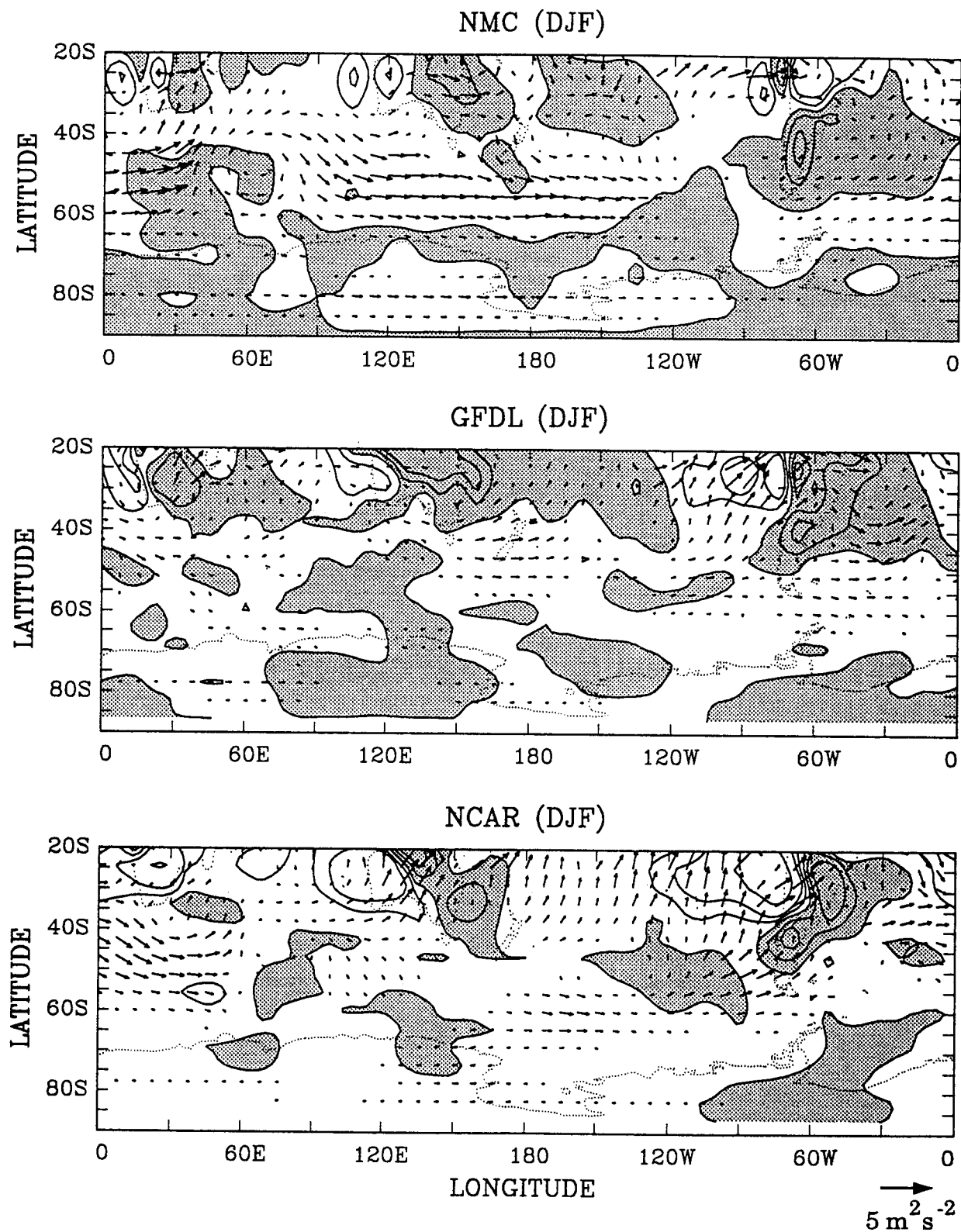


FIG. 12. As in Fig. 10 but for Southern Hemisphere DJF.

of stationary waves, the strongest forcing of F_s occurs during winter in the Northern Hemisphere, where three sources of F_s are prominent: eastern Asia, northeastern Pacific Ocean, and northern Atlantic Ocean. In each region, F_s has its principal source near the surface, from which it emanates upward and eastward. Internal forcing of stationary waves through interaction with transient waves may occur in the Northern Hemisphere, but evidence for this behavior appears more clearly in the Southern Hemisphere storm track, where a region of diverging stationary wave activity flux coincides with a region of converging, upper-atmosphere transient wave activity flux. Antarctica also appears to play an important role in forcing stationary waves in the Southern Hemisphere, as suggested by numerical studies of James (1988) and Watterson and James (1992).

A portion of the Northern Hemisphere, winter flux is directed toward the subtropics, where in the more recent NMC analyses, evidence is found to support Held's (1983) suggestion that waves transporting energy equatorward might be reflected poleward at critical lines in the subtropics. The more recent analyses also show that the flux of stationary wave activity is much weaker during Northern Hemisphere summer (compared to winter), as might be expected, and that it tends to be directed downward, indicating an upper-atmosphere source for F_s . Edmon et al.'s (1980) stationary wave E-P fluxes for the zonally averaged, observed, summer atmosphere show similar downward propagation.

The models fare best when the stationary wave forcing is strongest, that is, in the wintertime Northern Hemisphere, where they produce three surface sources of upward F_s with locations corresponding to the observed. For the Northern Hemisphere summer and the Southern Hemisphere in both summer and winter, the models show less agreement with observations, although they do simulate the generally downward flux of the observed, Northern Hemisphere summer, indicating that the physics responsible for the observed flux is contained in the models. Further analysis reveals that the most likely source of this wave activity flux is extratropical convection.

An implication of the model-observation comparison by Palmer et al. (1986) is that reasonable simulation of Northern Hemisphere stationary waves using the resolution of the models studied here (R15) results in part from a compensation of errors between weak momentum flux convergence from poorly resolved transient eddies and missing gravity-wave drag. The comparison here suggests an additional fortuitous cancellation of errors. During Northern Hemisphere winter over eastern Asia, weak topographic forcing due to spectrally smoothed orography may be compensated for by excessive diabatic forcing from latent heat release. Increasing model resolution should reduce orographic smoothing, but it will not necessarily improve simulations of diabatic processes. Coupling this infor-

mation with the apparent importance of convection as a stationary wave forcing mechanism during Northern Hemisphere summer, we conclude that attaining a more accurate simulation of stationary waves requires a much better understanding of the physics governing water vapor condensation and storm track maintenance.

Acknowledgments. We thank Drs. S. Manabe and W. Washington for providing us with the model output, Drs. P. Arkin and D. Gutzler for the NMC analyses, and Dr. C.-K. Park for the data used in Figs. 1 and 2. We also thank Drs. A. Plumb and R. Black for helpful discussions and the reviewers for their comments. This study was supported by the Carbon Dioxide Research Program of the U.S. Department of Energy under Grants DE-FG02-86-ER60422 and DE-FG02-92-ER61473.

REFERENCES

- Black, R. X., and R. M. Dole, 1993: The dynamics of large-scale cyclogenesis over the North Pacific Ocean. *J. Atmos. Sci.*, **50**, 421–442.
- Blackmon, M. L., R. A. Madden, J. M. Wallace, and D. S. Gutzler, 1979: Geographical variations in the vertical structure of geopotential height fluctuations. *J. Atmos. Sci.*, **36**, 2450–2466.
- Boer, G. J., and T. G. Shepherd, 1983: Large-scale two-dimensional turbulence in the atmosphere. *J. Atmos. Sci.*, **40**, 164–184.
- Branscome, L. E., and W. J. Gutowski, 1992: The impact of double CO_2 on the energetics and hydrologic processes of mid-latitude transient eddies. *Climate Dyn.*, **7**, 29–37.
- Chen, T.-C., and W. Baker, 1986: Global diabatic heating during FGGE SOP-1 and SOP-2. *Mon. Wea. Rev.*, **114**, 2578–2589.
- Edmon, H. J., B. J. Hoskins, and M. E. McIntyre, 1980: Eliassen-Palm cross-sections for the troposphere. *J. Atmos. Sci.*, **37**, 2600–2616.
- Grotch, S. L., and M. C. MacCracken, 1991: The use of general circulation models to predict regional climate change. *J. Climate*, **4**, 286–303.
- Gutowski, W. J., D. S. Gutzler, and W.-C. Wang, 1991: Surface energy balances of three general circulation models: Implications for simulating regional climate change. *J. Climate*, **4**, 121–134.
- Held, I. M., 1983: Stationary and quasi-stationary eddies in the extratropical troposphere. *Large-Scale Dynamical Processes in the Atmosphere*, B. Hoskins, and R. Pearce, Ed., Academic Press, 127–168.
- , and M. Ting, 1990: Orographic versus thermal forcing of stationary wave: The importance of the mean low-level wind. *J. Atmos. Sci.*, **47**, 495–500.
- Hoerling, M. P., T. K. Schaack, and D. R. Johnson, 1990: Heating distributions from January and July simulations of the NCAR Community Climate Models. *J. Climate*, **3**, 417–434.
- Hoskins, B. J., and D. J. Karoly, 1981: The steady linear response of a spherical atmosphere to thermal and orographic forcing. *J. Atmos. Sci.*, **38**, 1179–1196.
- , and P. J. Valdes, 1990: On the existence of storm-tracks. *J. Atmos. Sci.*, **47**, 1854–1864.
- Houghton, J. T., G. J. Jenkins, and J. J. Ephraums, Eds., 1990: *Climate Change: The IPCC Scientific Assessment*. Cambridge University Press, 365 pp.
- James, I. N., 1988: On the forcing of planetary-scale Rossby waves by Antarctica. *Quart. J. Roy. Meteor. Soc.*, **114**, 619–637.
- Kang, I.-S., and I. M. Held, 1986: Linear and nonlinear diagnostic models of stationary eddies in the upper troposphere during Northern summer. *J. Atmos. Sci.*, **43**, 3045–3057.

- Karoly, D. J., R. A. Plumb, and M. Ting, 1989: Examples of the horizontal propagation of quasi-stationary waves. *J. Atmos. Sci.*, **46**, 2802–2811.
- Kellogg, W. W., and Z.-C. Zhao, 1988: Sensitivity of soil moisture to doubling of carbon dioxide in climate model experiments. Part I: North America. *J. Climate*, **1**, 348–366.
- Kutzbach, J. E., and P. E. Guetter, 1986: The influence of changing orbital parameters and surface boundary conditions on climate simulations for the past 18 000 years. *J. Atmos. Sci.*, **43**, 1726–1759.
- Lau, N.-C., G. H. White, and R. L. Jenne, 1981: Circulation statistics for the extratropical Northern Hemisphere based on NMC analyses. NCAR Technical Note NCAR/TN-171+STR, National Center for Atmospheric Research, 138 pp.
- Malone, R. C., E. J. Pitcher, M. L. Blackmon, K. Puri, and W. Bourke, 1984: The simulation of stationary and transient geopotential-height eddies in January and July with a spectral general circulation model. *J. Atmos. Sci.*, **41**, 1394–1419.
- Manabe, S., and D. G. Hahn, 1981: Simulation of atmospheric variability. *Mon. Wea. Rev.*, **109**, 2260–2286.
- , and R. T. Wetherald, 1987: Large-scale changes of soil wetness induced by an increase in atmospheric carbon dioxide. *J. Atmos. Sci.*, **44**, 1211–1236.
- Mitchell, J. F. B., and C. A. Senior, 1989: The antarctic winter; simulations with climatological and reduced sea-ice extents. *Quart. J. Roy. Meteor. Soc.*, **115**, 225–246.
- Murphree, T., J.-M. Chen, P. Harr, and R. Gelaro, 1991: Short-term climate variations in the PNA region: The role of South Asia—tropical West Pacific heating anomalies. *Proc. Fifth Conf. on Climate Variations*, Denver, Colorado, Amer. Meteor. Soc., 340–343.
- Oort, A. H., 1983: *Global Atmospheric Circulation Statistics, 1958–1973*. U.S. Department of Commerce, 180 pp.
- Palmer, T. N., G. J. Shutts, and R. Swinbank, 1986: Alleviation of a systematic westerly bias in general circulation and numerical weather prediction models through an orographic gravity wave drag parameterization. *Quart. J. Roy. Meteor. Soc.*, **112**, 1001–1039.
- Pitcher, E. J., R. C. Malone, V. Ramanathan, M. L. Blackmon, K. Puri, and W. Bourke, 1983: January and July simulations with a spectral general circulation model. *J. Atmos. Sci.*, **40**, 580–604.
- Plumb, R. A., 1985: On the three-dimensional propagation of stationary waves. *J. Atmos. Sci.*, **42**, 217–229.
- , 1986: Three-dimensional propagation of transient quasi-geostrophic eddies and its relationship with the eddy forcing of the time-mean flow. *J. Atmos. Sci.*, **43**, 1657–1678.
- Randel, W. J., and D. L. Williamson, 1990: A comparison of the climate simulated by the NCAR Community Climate Model (CCM1:R15) with ECMWF analyses. *J. Climate*, **3**, 608–633.
- Rosen, R. D., and W. J. Gutowski, 1992: Response of zonal winds and atmospheric angular momentum variations to a doubling of CO₂. *J. Climate*, **5**, 1391–1404.
- Schlesinger, M. E., and J. F. B. Mitchell, 1987: Climate model simulations of the equilibrium climatic response to increased carbon dioxide. *Rev. Geophys.*, **25**, 760–799.
- Schubert, S., J. Pfendtner, and R. Rood, 1993: An assimilated dataset for earth science applications. *Bull. Amer. Meteor. Soc.*, **73**, 2331–2342.
- Shepherd, T. G., 1993: A unified theory of available potential energy. *Atmosphere–Ocean*, **31**, 1–26.
- Trenberth, K. E., 1991: Storm tracks in the Southern Hemisphere. *J. Atmos. Sci.*, **48**, 2159–2178.
- , and J. G. Olson, 1988: An evaluation and intercomparison of global analyses from the National Meteorological Center and the European Centre for Medium-Range Weather Forecasts. *Bull. Amer. Meteor. Soc.*, **69**, 1515–1524.
- van Loon, H., and R. L. Jenne, 1972: Zonal harmonic standing waves in the Southern Hemisphere. *J. Geophys. Res.*, **77**, 992–1003.
- Wallace, J. M., and D. S. Gutzler, 1981: Teleconnections in the geopotential height field during the Northern Hemisphere winter. *Mon. Wea. Rev.*, **109**, 784–812.
- Washington, W. M., and G. A. Meehl, 1984: Seasonal cycle experiment on the climate sensitivity due to a doubling of CO₂ with a general circulation model coupled to a simple mixed layer ocean model. *J. Geophys. Res.*, **89**, 9475–9503.
- Watterson, I. G., and I. N. James, 1992: Baroclinic waves propagating from a high-latitude source. *Quart. J. Roy. Meteor. Soc.*, **118**, 23–59.
- Webster, P. J., 1981: Mechanisms determining the atmospheric response to sea surface temperature anomalies. *J. Atmos. Sci.*, **38**, 554–571.
- , 1982: Seasonality in the local and remote atmospheric response to sea surface temperature anomalies. *J. Atmos. Sci.*, **39**, 41–52.